

Mass Accommodation Coefficient of Water: Molecular Dynamics Simulation and Revised Analysis of Droplet Train/Flow Reactor Experiment

Akihiro Morita*,†

Department of Chemistry, Graduate School of Science, Kyoto University, Kitashirakawa, Sakyo-ku, Kyoto 606-8502, Japan

Masakazu Sugiyama

Department of Electronics Engineering, School of Engineering, The University of Tokyo, 7-3-1 Hongo, Bunkyo-ku, Tokyo 113-8656, Japan

Hirofumi Kameda and Seiichiro Koda‡

Department of Chemical System Engineering, School of Engineering, The University of Tokyo, 7-3-1 Hongo, Bunkyo-ku, Tokyo 113-8656, Japan

David R. Hanson

Atmospheric Chemistry Division, National Center for Atmospheric Research, Boulder, Colorado 80303-2000

Received: April 18, 2003; In Final Form: February 10, 2004

The mass accommodation (condensation) coefficient α of water vapor into liquid water was theoretically studied via two complementary approaches: by molecular dynamics (MD) scattering simulation and by computational fluid dynamics simulation of the droplet train/flow reactor experiment. The MD scattering simulation predicts $\alpha \sim 1$ at 273 K. The fluid dynamics simulation quantitatively interprets the gaseous resistance in the droplet train flow tube, which demonstrated that the results of the droplet train/flow reactor experiment [Li et al., *J. Phys. Chem. A* **2001**, 105, 10627] are consistent with a value for the water α in the range between 0.2 and 1. Both methods are thus seen to be consistent and provide values for the mass accommodation coefficient of water in the ideal situation free from surface impurities and nonequilibrium latent heat production.

1. Introduction

In the mass transfer kinetics at gas/liquid interfaces, the mass accommodation coefficient α ($0 \leq \alpha \leq 1$) is defined as the probability that a gas molecule impinging on liquid surface is absorbed into bulk liquid. In particular, α for water vapor into liquid water, often called the condensation coefficient for water, is a fundamental kinetic parameter that reflects the microscopic efficiency of interfacial mass transfer. The value of α is used to predict the condensation and growth rate of water droplets in the atmosphere.^{1–4}

However, previous experimental measurements of the condensation coefficient yield values of the water α that are mutually inconsistent and that range over 3 orders of magnitude.^{1,5} The reasons for these experimental disagreements have not been fully elucidated, yet it has been generally observed that the water α for dynamically renewing water surfaces exceeds 0.1, while α for stagnant surfaces is below 0.1, presumably because of surface impurities in the latter.^{1,3–6} While the microscopic interpretation of the mass accommodation

kinetics/dynamics involving surface impurities is an interesting problem, in the present paper we focus on the water α for a fresh water surface. There is a well-known and more general problem that can afflict the previous experiments. Most researchers have derived the water α from measurements of the net condensation rates to liquid water in nonequilibrium conditions.^{1–5} Although these experimental conditions can be relevant to the rates of droplet growth in nonequilibrium situations, latent heat could bring considerable uncertainty into the derived α , as interfacial mass transfer is coupled with the heat transfer.^{3,7} Net latent heat production at the interface possibly facilitates re-evaporation and thereby could result in an underestimate of the condensation coefficient. Therefore, the above two sources of experimental uncertainties, i.e. surface impurities and latent heat, both tend to reduce a measured α , unless proper correction is made.

Recently the above two uncertainties have been ingeniously circumvented using the droplet train/flow reactor technique.⁸ This technique utilizes constantly refreshed water surfaces and provides an uptake measurement by precisely controlling surface area and interaction time. Li et al. isotopically labeled a fraction of gas-phase water to distinguish the “solute” molecules to be monitored, and thereby performed an uptake measurement of water into liquid water. Since their measurements are generally performed under saturated water vapor pressure, the nonequilibrium effect associated with latent heat is minimized. They

* Corresponding author. Fax: +81-564-55-7025. E-mail: amorita@ims.ac.jp.

† Present address: Institute for Molecular Science, Myodaiji, Okazaki 444-8585, Japan.

‡ Present address: Department of Chemistry, Faculty of Science and Technology, Sophia University, 7-1 Kioicho, Chiyoda-ku, Tokyo 102-8554, Japan.

reported $\alpha = 0.23 \pm 0.02$ for the mass accommodation of H_2^{17}O into liquid water at $T = 0^\circ\text{C}$, which is still considerably smaller than unity.

The liquid–vapor interfacial structure and properties of water have been extensively studied by molecular dynamics (MD) simulations.^{9–14} MD calculations of direct scattering and/or free energy calculations^{15–23} enable the exploration of the mass accommodation dynamics at the molecular level, with very little ambiguity in the interpretation of the calculated data. For strongly interacting systems such as hydrogen bonding, previous MD calculations suggest that the mass accommodation coefficients are generally close to unity for thermal collisions near room temperature,^{17–19,22,23} whereas they are considerably smaller than unity when the collision energy is as large as 30–80 kJ/mol.¹⁶ In the latter case, direct comparison of the MD calculations with surface scattering experimental results is available,²⁴ and it was demonstrated that the MD calculations reproduce very well the mass accommodation coefficients and the energy loss upon a straightforward choice of potential functions.

However, when the collision energy is thermal ($k_{\text{B}}T \sim 2.3$ kJ/mol at $T = 273$ K) and a substantial vapor pressure is present, the corresponding scattering experiments are virtually infeasible, since the vapor prevents the incident gas molecules from direct collision to the surface. We are left, then, with comparisons of α from the MD calculations to the less direct measurements of α obtained from phenomenological uptake coefficients, with proper correction for the other kinetic elements involved in the mass transfer rate, such as gas-phase diffusion, and liquid-phase solubility, etc. As evidenced by the wide range in α for water from the experimental results discussed previously, this can involve much uncertainty. The droplet train flow reactor is the preferred experiment with which to compare, for the reasons listed above. Yet earlier comparisons for the uptake of ethanol into liquid water, as an example of a hydrogen bonding system, the MD simulation,^{17,19} and the droplet train/flow reactor experiment,^{25–27} have provided apparently inconsistent mass accommodation coefficients. The reasons for the inconsistency are not clear yet,²³ but one conceivable reason lies in the uncertainties in the corrections to the phenomenological uptake rates.

In the droplet train/flow reactor experiment, as well as in many other heterogeneous kinetics experiments, α is derived from the uptake coefficient γ , which represents the experimental mass transfer rate normalized to the ideal thermal collision rate. According to the resistance model,²⁸ α and γ are related via

$$\frac{1}{\gamma} = \frac{1}{\Gamma_{\text{g}}} + \frac{1}{\alpha} + \frac{1}{\Gamma_{\text{sol}}} \quad (1)$$

where $1/\Gamma_{\text{g}}$ is the gas-phase diffusion resistance and $1/\Gamma_{\text{sol}}$ is the liquid-phase solubility resistance. Equation 1 indicates that both $1/\Gamma_{\text{g}}$ and $1/\Gamma_{\text{sol}}$ have to be precisely evaluated to derive α from γ , unless these two resistances are negligibly small compared to $1/\alpha$. Accordingly, the droplet train/flow reactor experiments generally employ conditions of low pressure and short interaction times to minimize $1/\Gamma_{\text{g}}$ and $1/\Gamma_{\text{sol}}$, respectively. For the mass accommodation of water vapor into liquid water results, the solubility resistance $1/\Gamma_{\text{sol}}$ is thought to be negligible.⁸ Later, in comparisons with the measured uptake rates, we will attempt to assess the effect of a finite solubility on the uncertainty in the experimental result. For the gas-phase diffusion resistance, however, a practical difficulty arises in minimizing $1/\Gamma_{\text{g}}$, since a desirable low-pressure condition is

limited by the substantial water vapor pressure. In such a case, precise estimation of $1/\Gamma_{\text{g}}$ is particularly crucial for evaluating α .

The term $1/\Gamma_{\text{g}}$ in the droplet train flow tube is usually estimated by using the Fuchs–Sutugin formula²⁹ with an empirical correction where the Knudsen number (Kn) is replaced by an effective Kn, Kn^* , calculated using an effective diameter.^{30–32} The Fuchs–Sutugin formula provides the gaseous uptake rate over a wide range of Kn for spherical boundary conditions. It was developed for uptake onto a single spherical droplet immersed in a quiescent gas. It is not conceptually straightforward to apply this formula to the actual droplet train/flow reactor experiments, where a train of droplets is moving rapidly through the carrier gas in a flow reactor. For this reason, we have performed a quantitative evaluation of $1/\Gamma_{\text{g}}$ via computational fluid dynamics simulations using the experimental boundary conditions that are typical for the droplet train flow reactor.^{33,34} The calculations revealed that the effects of the flow field and the interference in the uptake between droplets in the droplet train are, in fact, quite remarkable. We were able to confirm that these effects are qualitatively taken into account by the empirical correction for the Fuchs–Sutugin formula. However, an important quantitative finding was that the accuracy of the empirical correction needs to be further improved, especially when a precise value for $1/\Gamma_{\text{g}}$ is required.

In this study, we will theoretically evaluate the mass accommodation coefficient of water, both via the molecular dynamics simulations of direct scattering and via the fluid dynamics calculations for the gas-phase diffusion resistance in the droplet train flow tube. We think that the combination of these two approaches are complementary and it will benefit the understanding of the microscopic picture of mass accommodation processes. After the droplet train/flow reactor experiment of the water accommodation is re-interpreted with the numerical evaluation of the gas-phase resistance, and solubility concerns are outlined, the experimental result will be seen to have a fairly large uncertainty and allow for a unit α at 0°C , which is compatible with the MD calculations.

The remainder of this paper is constructed as follows. The next section discusses the microscopic scattering events of water molecules at liquid water surface as given by the MD simulation, and we thereby estimate the mass accommodation coefficient of water. Next, in section 3, we describe the fluid dynamics simulation of the droplet train flow tube to reexamine the precise experimental conditions reported for the mass accommodation of water measurements. In this section we show that a consistent picture of water accommodation can be obtained through the combination of the MD scattering simulation and a revised analysis of the droplet train/flow reactor experiment. Brief concluding remarks follow in section 4.

2. MD Scattering Simulation

2.1. MD Procedure. In the MD approach, evaluating α is conceptually straightforward. It simulates a large number of thermal scattering events of gaseous water molecules onto a liquid water surface, and the probability that the gas molecules will be absorbed into the liquid is statistically derived. In the present MD simulation, the liquid is modeled as a thin film of liquid water, as illustrated in Figure 1a, in combination with two-dimensional periodic boundary conditions along the *X* and *Y* axes. Accordingly, the liquid film spreads infinitely along the *X–Y* plane and has two sides exposed to the gas. The collision events take place at either gas–liquid interface. The lateral periodic length is set at $L = 31.0 \text{ \AA}$, and one periodic

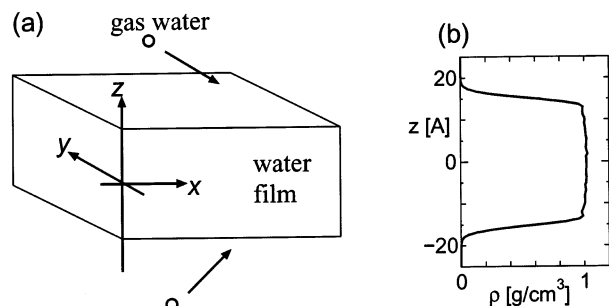


Figure 1. (a) Scheme of the MD scattering simulation. (b) Density profile of the liquid water film along the Z axis.

cell is set to initially contain 1000 water molecules. Consequently, the vertical thickness of the liquid film is approximately $\sim L$ along the Z axis, as a volume of L^3 would have 1000 water molecules at the bulk density, 1.00 g/cm^3 .

The MD calculations are carried out at a constant temperature of $T = 273 \text{ K}$ using the Nosé–Hover thermostat³⁵ with a damping constant of 0.4 ps . The force field of the water molecules is represented by the SPC/E model,³⁶ with fixed internal coordinates. The SPC/E model has been applied to the liquid–vapor interface of water with considerable success.^{13,14,22} Since the present study deals with thermal collisions, the collisions couple very little to the water internal vibrations. The long-range interactions are cut off at half the periodic length $L/2$. The time integration is performed by the velocity Verlet algorithm^{35,37} with a time step of 1 fs , and the orientational coordinates are treated by the quaternion representation.³⁷

To prepare the initial conditions of thermalized liquid water, we equilibrate the liquid film in two steps. First, the water molecules are confined in the region $-L/2 < Z < L/2$ by introducing two auxiliary hard walls at $Z = -L/2$ and $Z = L/2$, so that the density is fixed at 1.00 g/cm^3 , and the MD calculation is carried out for 50 ps under the constraint. Then the two auxiliary walls are removed and the equilibration run continues for another 50 ps . The density profile of the equilibrated liquid film at $T = 273 \text{ K}$ is shown in Figure 1b.

After the liquid is thermalized, a scattering simulation is carried out for 110 ps . During the scattering simulation, except for the last 10 ps , a water molecule is generated every 10 ps on alternating sides of the liquid about 15 Å from the surface.³⁸ The newly created molecule's orientation and X,Y coordinates are random, and its initial translational and rotational velocities are sampled from the Maxwell–Boltzmann distribution at $T = 273 \text{ K}$, on condition that the initial translational velocity along the Z axis points toward the liquid surface (i.e., the initial Z velocity v_z is set to be positive at $Z = -L/2 - 15 \text{ Å}$, or negative at $Z = L/2 + 15 \text{ Å}$). Therefore, during one MD run, $(110 \text{ ps} - 10 \text{ ps})/10 \text{ ps} = 10$ incident molecules are generated for the surface scattering, with the last 10 ps being a margin for the last one. Consequently, each colliding molecule has nearly 20 ps of relaxation time before the next incident molecule appears on its side of the liquid. We performed 100 different simulations, each with its own initial configuration using parallel computing. Thus the fate of 1000 incident molecules that were generated in the gas phase was studied. The mass accommodation coefficient α is statistically derived from these 1000 surface scattering trials.

2.2. MD Results. A typical trajectory of a scattering simulation is illustrated in Figure 2a, which displays a time evolution of the Z coordinates of all the constituent water molecules during 110 ps . The filled band in $-20 \text{ Å} \lesssim Z \lesssim 20 \text{ Å}$ corresponds to the liquid film and the 10 lines outside the band

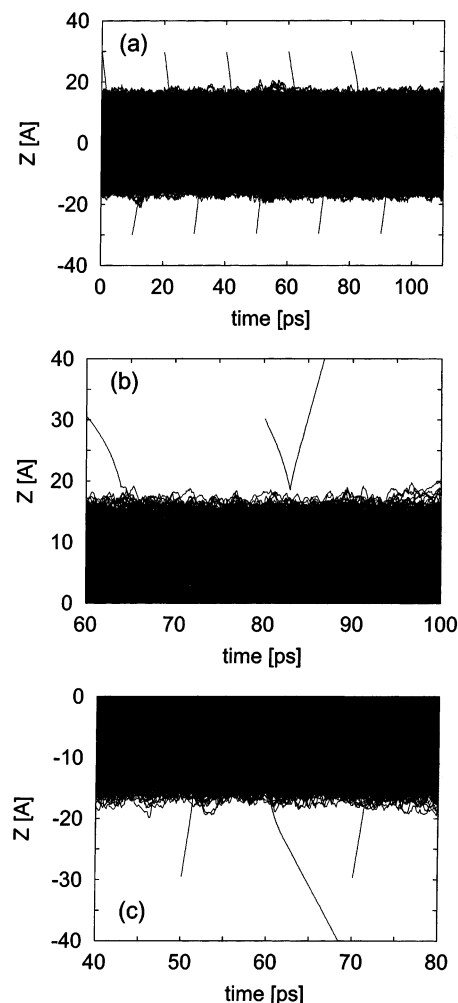


Figure 2. (a) Typical MD scattering trajectory for 110 ps , projected on the Z axis. (b, c) Magnified pictures illustrating recoil and evaporation events, respectively, in other trajectories.

designate the thermal surface scattering events of the generated molecules. Figure 2a shows that all 10 of the water molecules are absorbed upon contact with the liquid surface.

While most of the incident molecules were absorbed, on occasion we observed recoil events. Figure 2b shows an example of a recoil event, which is characterized by a nearly elastic collision and a residence time at the surface that is much less than a picosecond. Among the total of 100 independent simulations, three direct recoils were observed. Therefore, the mass accommodation coefficient α is determined to be $\alpha = (1000 - 3)/1000 = 0.997$, very close to unity. This is consistent with the previous MD study of Nagayama and Tsuruta.²² Matsumoto reported $\alpha \sim 0.4$ by his MD simulation,²¹ and we think that this should hold for metastable liquids of artificially low density.²³

During the MD scattering simulation, we observed the evaporation of a total of four molecules. Figure 2c illustrates an example of the evaporation; note that the evaporating molecule is not one of the incident molecules. While some water molecules may thermally evaporate during the time evolution, it is not straightforward to distinguish the fully thermal evaporation from the exchange evaporation induced by the accommodation of impinging molecules. If the observed evaporation is assigned to the latter, it may be counted as a recoil in the microscopic definition of the mass accommodation coefficient.²³ Therefore, a lower limit to the calculated mass

accommodation coefficient could be $\alpha = (1000 - 7)/1000 = 0.993$. Considering this uncertainty, the calculated α is in the range of $0.993 \leq \alpha \leq 0.997$. The uncertainty due to the exchange/evaporation is thought to be less than that discussed here, as argued further in the next subsection.

2.3. Discussion. One advantage of the MD simulation is the absence of collisions of the incident molecule with other gaseous molecules, even under the conditions where a substantial vapor pressure would be expected. This is because the typical mean free path l for the incident molecule is several orders of magnitude longer than the dimension of the simulation L . For the water vapor pressure of 611.3 Pa at $T = 0^\circ\text{C}$ ³⁹ and in the absence of air, the diffusion coefficient of water D is calculated to be $D = 2.4 \times 10^{-3} \text{ m}^2/\text{s}$ by the CHEMKIN package,⁴⁰ as described later in section 3.1. Hence l is estimated by Meyer's expression as $l = 3D/\bar{c} = 1.3 \times 10^{-5} \text{ m}$, where $\bar{c} = 567 \text{ m/s}$ is the average thermal velocity of a water molecule at $T = 273 \text{ K}$. Even in one atmosphere of air, where D is estimated to be $1.9 \times 10^{-5} \text{ m}^2/\text{s}$, the mean free path of a water vapor molecule $l = 1.0 \times 10^{-7} \text{ m}$ is still much longer than L . Therefore, collisions of incident molecules with other gaseous molecules are safely neglected in the present simulation.

Another concern is the amount of energy absorbed by the liquid due to the frequency of the surface collisions. The interval between incident molecules is 20 ps which is sufficiently longer than the energy relaxation time (~ 10 ps) after surface accommodation that was deduced for a hydrogen bonding system.¹⁷ Therefore, successive collisions during the simulation are considered to be independent events. Also, the interval between collisions of gaseous species with the L^2 surface area is ~ 1000 ps in the experimental situation, which is estimated using the gas-kinetic equation and a total pressure of 20 Torr.

In evaluating the mass accommodation coefficient, there are two sources for the error bars; one is the statistical uncertainty, and the other is the uncertainty associated with the definition of thermal/exchange evaporation as discussed in section 2.2. The statistical uncertainty of α derived from all the simulations is estimated by dividing them into 10 segments and then calculating the α values separately. The root-mean-square deviation among the 10 values of α was found to be 0.0046. The latter uncertainty arises from the four evaporation events, as exemplified in Figure 2c. Although the example shown in Figure 2c appears to be a pure thermal evaporation, rigorous distinction between thermal and exchange evaporation can be difficult in other cases. One can estimate the expected number of thermal evaporation events, assuming detailed balance between condensation and evaporation fluxes and an evaporation coefficient of 1. The maximum evaporation flux is given by the gas-kinetic collision flux, $n_g \bar{c}/4$. Therefore, the average number of the thermal evaporation events expected during 11000 ps of simulation from both sides of the liquid $2L^2$ is expected not to exceed

$$(n_g \bar{c}/4) \cdot 2L^2 \cdot 110 \text{ ps} \times 100 = 4.9 \quad (2)$$

This estimate is consistent with the number of observed evaporation events. We conclude that the MD scattering simulation yields the mass accommodation coefficient for thermal uptake of water into liquid water to be $\alpha > 0.99$ at $T = 273 \text{ K}$, very close to unity.

3. Gas-Phase Analysis of the Droplet Train/Flow Reactor

In this section, we take a complementary approach to obtain a value for the mass accommodation coefficient of water, by

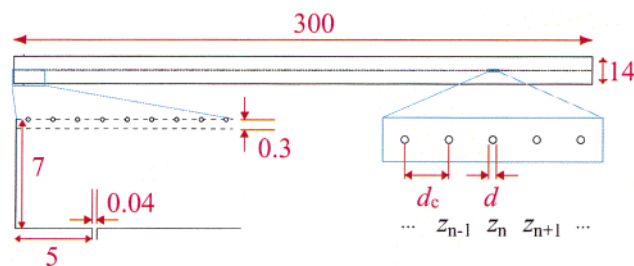


Figure 3. Cross sectional view of the cylindrical flow tube and the droplet train on the axis. Magnified views near the inlet (left side) and near the n th droplet are shown in the lower left corner and right corner, respectively. Unit: mm.

TABLE 1: Droplet Configurations in the Flow Tube

	orifice diameter $d_o/\mu\text{m}$	droplet diameter $d/\mu\text{m}$	droplet distance $d_c/\mu\text{m}$	orifice frequency ^a f_o/kHz	symbols in Figure 7
(A)	28	84	504	53.4 (1/4)	circle
(B)	28	133	2016	13.4 (1/16)	triangle
(C)	64	304	4608	5.9 (1/16)	square

^a Numbers in parentheses denote the ratios to the natural breakup frequency.

analyzing the droplet train/flow reactor experiment. As discussed in section 1, this technique avoids the ambiguities that most of the other measurements suffer from, and thus is potentially suitable to reveal microscopic mass accommodation kinetics/dynamics. However, a significant uncertainty is presumably in the calculation of the gas-phase resistance in the flow tube, which has usually been treated empirically. We discuss the gas-phase resistance via fluid dynamic calculations to evaluate the magnitude of this uncertainty.^{33,34}

3.1. Computational Method. The geometry and conditions of the fluid dynamics simulations of the flow reactor are chosen to imitate the experiment of Li et al.⁸ Figure 3 shows a schematic picture of the droplet train flow tube. The droplet train is located on the flow tube axis and moves at a velocity v_d from left to right, while the flow tube wall is fixed. The present simulation explicitly treats the droplets as moving so that a direct comparison with the experimental results is facilitated.⁴¹ Our previous simulation^{33,34} employed a fixed droplet train and a moving wall to model the moving droplets in the flow tube which complicates a direct comparison with experiment. The previous results are consistent with those of the present study.

In most of the calculations of this study, v_d was set to be 27 m/s, which is a typical experimental value. The droplet diameter d and the distance between the centers of the droplets d_c are determined from the orifice diameter d_o and vibrating frequency f_o as

$$\frac{\pi d^3 f_o}{6} = \frac{\pi d_o^2 v_d}{4}, \quad v_d = f_o d_c \quad (3)$$

Table 1 lists the three configurations (A)–(C) that were employed in the present simulation. In each case, the orifice frequency f_o was set to a subharmonic of the natural breakup frequency, $v_d/4.5d_o$.³⁰ To explore the effect of droplet speed, we also examined $v_d = 16$ and 44 m/s by varying the orifice frequency in case (B) with the other conditions fixed.

The total mass flow rate of carrier gas (water vapor plus noble gas) was $F_g = 4.6 \text{ STP cm}^3/\text{s}$ (273 K, 1 atm), which traveled in the same direction as the droplets. This gives an average gas velocity v_g that ranged from 3.80 m/s (273 K, 6 Torr) to 1.14 m/s (273 K, 20 Torr). The gas flow entering the reactor was assumed to be laminar and thus the radial velocity profile was



Figure 4. Concentration field (upper panel) and streamlines (lower panel) in the flow tube. The two pictures show half cross section of the upstream region; upper and lower boundaries of each panel correspond to the flow tube wall and axis, respectively. The droplet configuration (A) in Table 1 is employed with the total pressure of 6 Torr and He buffer. $\alpha = 1$ is assumed on the droplet surface.

TABLE 2: Ambient Conditions in the Flow Tube

total pressure ^a /Torr	carrier gas	diffusion coefficient of H ₂ ¹⁷ O/10 ⁻³ m ² s ⁻¹
6	He	2.26
13	He	1.79
20	He	1.48
13	Ar	0.99
20	Ar	0.66

^a Total pressure contains saturated H₂O vapor (4.6 Torr).

set to be parabolic at the inlet (left edge of Figure 3). Figure 3 shows a side loop inlet 5 mm downstream of the main flow inlet, from which the trace gas, in a tenth of the total gas flow, can be injected into the main flow with a radial velocity of that is 10 times the main average axial velocity.⁴² The side inlet flow can perturb the overall flow, and its influence on the uptake kinetics can be examined by comparing the simulation with the side inlet to that without the side inlet. In the latter case, the trace species is injected with the main flow.

The calculations are carried out for isothermal conditions at 0 °C. In the experiment by Li et al.,⁸ the uptake of a small amount of isotopically labeled water (H₂¹⁷O) was measured. Accordingly, in the present simulation, the gas initially contained H₂¹⁷O at a typical experimental concentration of 2×10^{13} molecules/cm³ (5.7×10^{-4} Torr), in addition to normal H₂O. (When the side inlet was employed, the initial H₂¹⁷O concentration in the second flow was set 10 times higher than this to realize a comparable initial concentration after dilution.) The ambient gas consists of the saturation vapor pressure of water (4.6 Torr) and an inert carrier gas, either He or Ar, at variable partial pressures to thereby attain a variable Knudsen number (Kn). For each droplet configuration (A)–(C) in Table 1, five ambient conditions in Table 2 were applied. The diffusion coefficient of H₂¹⁷O in the mixture, D , was estimated based on the dilute approximation³¹ and using binary diffusion coefficients estimated with the CHEMKIN transport package.⁴⁰ Viscosities of the component gases are also estimated with CHEMKIN, and the overall viscosity is derived by averaging those with the weight of their mole fractions. The transport properties of H₂¹⁷O are assumed to be identical to those of H₂O.

The uptake flux of H₂¹⁷O onto the droplet surface is modeled as $R = k_s C_s$, where C_s is the H₂¹⁷O concentration in the vicinity of the surface, and k_s is the rate constant of accommodation. The term k_s as a function of α is given by⁴³

$$k_s = \frac{\bar{c}}{4} \frac{\alpha}{1 - \alpha/2} \quad (4)$$

where \bar{c} is the average thermal velocity of H₂¹⁷O and α is the mass accommodation coefficient, which is an input parameter of the calculations. It was assumed to be either $\alpha = 1$ or 0.23, the two values in question. To examine how the uptake coefficient γ changed as the input α was varied, we also calculated γ while varying α stepwise for one set of experimental conditions (see Figure 9 later).

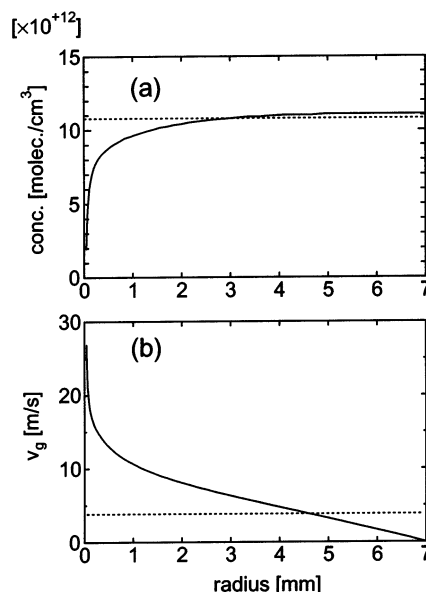


Figure 5. Radial profiles of (a) concentration and (b) gas velocity at $Z = 20$ cm. The horizontal dotted lines denote the radially average values at this cross section. The geometry and ambient conditions are same as in Figure 4.

The computational fluid dynamics calculations were carried out using the FLUENT ver. 6 suite,⁴⁴ with the assumption of an axisymmetric 2-dimensional configuration. Half of the axial cross sectional plane was divided into 190,000–240,000 meshes. To represent the moving droplets, the grids inside the tube were divided into two parts: the inner cylindrical region that extends out to a radius of 0.3 mm and the remaining outer annulus region. The inner region includes the droplets and its meshes move along with them at v_d . The outer region has stationary meshes that are fixed to the tube wall. Continuity conditions were imposed on all the variables at the virtual boundary ($r = 0.3$ mm) dividing the inner moving meshes from the outer stationary ones. Accordingly, the axial gas velocity at the droplet surface, as measured in the wall-fixed coordinate, will be v_d and at the tube wall it will be 0 (see Figure 5b).

3.2. Results and Discussion. 3.2.1 Concentration and Flow Fields. Figure 4 displays a concentration field and streamlines for a typical set of conditions. The solute species, injected from the side inlet, readily mixes into the main flow, and then its concentration decreases downstream due to the droplet sinks along the axis (located at the lower bound of each panel in Figure 4). The streamlines near the inlet region indicate that the second flow from the side inlet, carrying 10% of the total mass flow, does not strongly perturb the main laminar flow.

The radial profiles of concentration and axial velocity in the downstream region ($Z = 20$ cm) are depicted in Figure 5. The concentration of the solute species is strongly depleted near the axis, as shown in panel (a). In the velocity profile of panel (b),

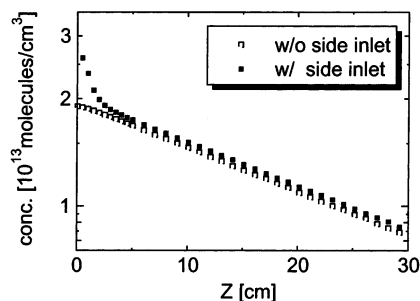


Figure 6. Axial concentration decay in the flow tube equipped with the side inlet (solid symbols) and without the side inlet (open symbols). The geometry and ambient conditions are same as in Figure 4.

shear friction by the moving droplets is apparent near the axis, which distorts the parabolic shape of the background laminar flow.

In the experimental analysis, the decrease in the gas-phase concentration of the solute species is monitored as the interaction length (and droplet configuration) along the tube axis is varied. Accordingly, Figure 6 shows the radially averaged gas-phase concentration as a function of the axial position Z . The concentration profile derived from Figure 4 (solid symbols) is compared to that without the side inlet (open symbols), where the droplet geometry and ambient conditions are the same except for the inlet configuration. We find that the transient anomaly dies away in a few cm and the downstream region is well represented by an exponential curve for both cases. The exponential decrease is consistent with the experimental results for a varying interaction length. In comparing the solid symbols with the open ones, Figure 6 indicates that the second flow injected from the side inlet does little to alter the exponential slope. Therefore, we will use data (excluding the first few cm) from the simulations without the side inlet to compute the exponential decay constant and its dependence on droplet configuration and ambient conditions.

3.2.2. Calculation of Uptake Coefficient. The exponential portion of the solute concentration decay is given by the first-order equation

$$\frac{dC(Z)}{dZ} = -k_{ov}C(Z) \quad (5)$$

where $C(Z)$ is the radially averaged concentration at Z and k_{ov} is the phenomenological axial decay constant for the concentration profile. In the conventional analysis based on the plug flow approximation, k_{ov} is related to the calculated uptake coefficient γ_{calc} as follows:

$$k_{ov} = \frac{1}{F_g} \frac{\pi d^2 \bar{c}}{d_c} 4\gamma_{calc} \quad (6)$$

F_g is the gas volume flow rate at the experimental temperature and pressure. The second term $\pi d^2/d_c$ is the droplet surface area per unit length along the flow tube axis.

We note that our simulations are based on the continuum description, and this could lead to an artificial overestimate of the exponential decay constant in the high Kn region. This is accounted for by normalizing the results to the kinetic correction based on the Fuchs–Sutugin formula and its continuum limit

$$\gamma = \frac{0.75/Kn - 1/2 + 1/\alpha}{(0.75 + 0.283Kn)/(Kn(1 + Kn)) + 1/\alpha} \gamma_{calc} \quad (7)$$

In the above equation, Kn is the geometric Knudsen number,

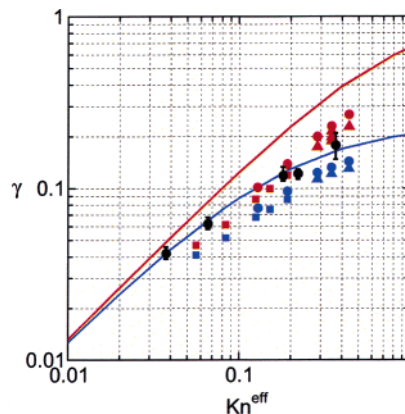


Figure 7. Uptake coefficients of water γ as a function of the effective Knudsen number Kn^{eff} . Black symbols with error bars denote the experimental values of $H_2^{17}O$ by Li et al.⁸ (Copyright 2001, American Chemical Society.) Circles, triangles and squares are calculated values using the geometries A–C listed in Table 1, respectively. Red symbols correspond to $\alpha = 1$ assumed, and blue to $\alpha = 0.23$. The curves denote the empirical Fuchs–Sutugin formula, eq 8, with assuming $\alpha = 1$ (red) and 0.23 (blue).

$Kn = 2\lambda/d$, where $\lambda (= 3D/\bar{c})$ is the mean free path of a $H_2^{17}O$ molecule and d is the droplet diameter. α is the “true” mass accommodation coefficient in eq 4, which is an input for the fluid dynamics calculations.

The kinetic correction factor in eq 7 makes use of the Fuchs–Sutugin formula, which was derived for uptake onto a single isolated droplet, in the intermediate transport region. We assume that eq 7 can be applied to the droplets in the droplet train flow tube. The kinetic collision effect is a local phenomenon that takes place on the order of a molecular mean free path from the surface which is typically $0.1d$ for the present simulations. This is much shorter than the droplet interference effect which occurs for droplet spacings that are 2 to 5 droplet diameters. Though the Fuchs–Sutugin formula in principle cannot be expected to apply to the droplet train as a whole, the kinetic correction effect in the vicinity of the surface is thought to be essentially independent of the proximity of other droplets. To the extent that this might introduce systematic deviations, we note that this correction was generally only a few percent and at most 5%.

Figure 7 summarizes the calculated data for γ as a function of droplet configuration A–C (Table 1), assumed α ($= 1$ or 0.23), and ambient conditions (Table 2). The varying ambient conditions are represented in the abscissa of Figure 7 using the effective Knudsen number, defined as $Kn^{eff} = 2\lambda/(2.0d_o)$, where the droplet diameter d is replaced with $2.0d_o$.^{30–32} Since the experimental data of Li et al.⁸ were plotted using the effective Knudsen number, we employed it here for convenience of comparison. The experimental data seem to compare better to the numerical results where $\alpha = 1$ was assumed. The Li et al. data employ an experimental device of taking the difference between the kinetics derived from two different droplet configurations. This is taken into account and discussed in more detail below.

3.2.3. Uptake with Varying Configuration and Droplet Speed.

Before a detailed comparison of the calculated data to the experimentally derived results, we give a brief discussion of the calculated data. Figure 7 indicates that the three configurations A–C, denoted by circles, triangles, and squares, yield similar γ at each set of α and Kn^{eff} , while the red symbols ($\alpha = 1$) and blue ones ($\alpha = 0.23$) are apparently distinguishable. The configurations A and B result in values for γ that are within

~15%. Whereas this is consistent with previous experimental observations that the measured uptake coefficient at a fixed d_o is insensitive to the orifice frequency f_o ,³⁰ this modest difference should be considered as part of the experimental uncertainty in deriving γ , as discussed in section 3.2.7.

We also examined the effect on γ of the droplet speed, by employing two other droplet velocities, $v_d = 16$ and 44 m/s at one set of conditions (case B, $\alpha = 1$, and $\text{Kn}^{\text{eff}} = 0.35$). The calculated γ at $v_d = 16$ m/s was 4.9% smaller than that at $v_d = 27$ m/s, while γ at $v_d = 44$ m/s was 6.4% larger than that at $v_d = 27$ m/s. While it is not surprising that a larger droplet speed facilitates transport, the effect on γ is relatively minor, which is consistent with the experimental observation.³⁰

3.2.4. Comparison with Empirical Fuchs–Sutugin Formula. Figure 7 also displays the experimental γ and the empirical expressions based on the Fuchs–Sutugin formula²⁹ with the effective Knudsen number^{8,30–32} as

$$\frac{1}{\gamma} = \frac{0.75 + 0.283\text{Kn}^{\text{eff}}}{\text{Kn}^{\text{eff}}(1 + \text{Kn}^{\text{eff}})} + \frac{1}{\alpha} \quad (8)$$

The red and blue curves in Figure 7 denote the empirical formula assuming $\alpha = 1$ and 0.23, respectively. Since the curve for $\alpha = 0.23$ appears to agree with the experimental data, Li et al.⁸ concluded that $\alpha = 0.23 \pm 0.02$ for mass accommodation of H_2^{17}O on water at 0 °C.

However, Figure 7 indicates that the empirical formulation systematically overestimates the γ calculated with the fluid dynamics simulations for both $\alpha = 1$ and $\alpha = 0.23$. The mechanism of the deviation has been discussed in detail in our previous study.^{33,34} In short, the analysis of the gas flow field showed that the solute-depleted regions in the vicinity of the droplets significantly overlap each other, since, qualitatively speaking, a given droplet runs after the wake of those preceding it, resulting in a reduced uptake efficiency compared to an isolated droplet. Although the reduced uptake efficiency is partly accounted for by the empirical modification of the Fuchs–Sutugin formula, the calculations indicate that the Fuchs–Sutugin empirical formula does not exactly account for gas-phase diffusion to a train of moving droplets.

Comparing the reported experimental γ to the calculations, one can see that the experimental γ are more consistent with the calculations for $\alpha = 1$ (red symbols) than for $\alpha = 0.23$ (blue symbols). Note also that the experimental γ in general exceed the calculated γ for $\alpha = 1$ for droplet configuration C using a different orifice diameter. The analysis of the droplet train data likely depends on experimental conditions, which should be further examined both experimentally and theoretically. When the gas-phase diffusion resistance is properly estimated, the droplet train/flow reactor experiment could be interpreted with a mass accommodation coefficient for H_2^{17}O that is substantially higher than 0.23.

3.2.5. Uncertainties in the Fluid Dynamics Simulation. Next, possible uncertainties in the present calculations are considered, since evaluating the error bar for γ is crucial for a meaningful comparison of the calculation and the experiment.

For the fluid dynamic simulations, possible sources of error include (1) that a discrete mesh division can affect the numerical solution of the fluid dynamics equations, (2) the calculated diffusion coefficients of the gas species, (3) droplet deceleration in the flow tube, (4) the internal liquid motion of the droplets, (5) a deviation from the continuum treatment in higher Kn region, and (6) the fitting accuracy of k_{ov} for the exponential concentration decay. We have discussed the issues 1–5 in detail

in the Appendix of our previous publication.³⁴ To summarize, we concluded that the calculated γ had an error range of $-15\% \sim +10\%$ in our previous simulation. The larger error in the negative direction was mainly attributed to issue 5 and to the previous configuration of our simulation of the flow tube that used a droplet-fixed arrangement.³⁴ The latter source of error (both negative and positive) is removed for the present simulations where the new flow tube configuration has a realistic length and a wall-fixed coordinate was employed. Here we deal with issues 5 and 6. The discussion of issues 1–4 in ref 34 is applicable to the present water uptake.

Issue 5 is associated with the limitation of the fluid dynamics simulation based on a continuum description. The systematic overestimation by the continuum description was accounted for by eq 7. Note that the correction factor in eq 7 is negligible (less than 1%) when $\text{Kn} < 0.1$, and smaller than 5% for all the data points in Figure 7. Note that the geometric Knudsen number based on the droplet diameter is properly used in eq 7.

Regarding problem 6, k_{ov} in eq 5 is determined by a least-squares fitting procedure of the axial concentration decay profile, as illustrated in Figure 6, except for a few cm region near the inlet. The uncertainty in the least-squares fitting is less than 1%, indicating that the decay of $C(Z)$ is very close to exponential. The problem 6 is shown to be a minor source of uncertainty.

From the above error analysis, we conclude that the fluid dynamics modeling and the accuracy of the numerical calculations are greatly improved in a quantitative sense from our previous estimate.³⁴ However, there remain a number of uncertainties in the analysis of both experiment and simulation, as discussed below.

3.2.6. Plug Flow Approximation. The plug flow approximation is a commonly used device in the analysis of flow reactor data as it reduces the gas flow issues to a one-dimensional problem along Z . As it is used in the droplet train flow reactor, we have accordingly employed it here to derive the uptake coefficient, γ_{calc} eq 6. It is not a direct source for the discrepancy between the experiment and simulation discussed above, however, it is worthwhile to explore the usefulness of this approximation. As illustrated in Figure 5, the real gas velocity profile and the reactant concentration are both not radially uniform, which is a violation of the plug flow approximation.⁴⁵ This issue might have possible importance for the accuracy (and precision) of the uptake coefficients obtained from either the experiment or the simulation. Here we analyze potential deviations from the plug flow approximation with the help of the fluid dynamics calculations.

When the flow is not radially uniform, the axial concentration decay slope does not necessarily coincide with the actual uptake rate into the droplets in a flow tube segment. This might complicate the analysis of the experimental and/or numerical results. Whereas the uptake amount is not usually measured by the experiments, it is readily computed in the fluid dynamics simulation from the definition of the measured uptake coefficient. The uptake coefficient is obtained by comparing the deposition rate to the droplets in a given flow tube segment with that given by the gas-kinetic equation where the radial average concentration in the flow tube segment is employed. This definition for γ is the starting point for the analysis of the droplet train flow reactor.³² Note that in our previous work,^{33,34} we employed this definition. To distinguish it from that used in the present work, we call it the “local γ ”. We compare it to the uptake coefficient derived from the axial decay slope using eq 6, which we call the “slope γ ”.

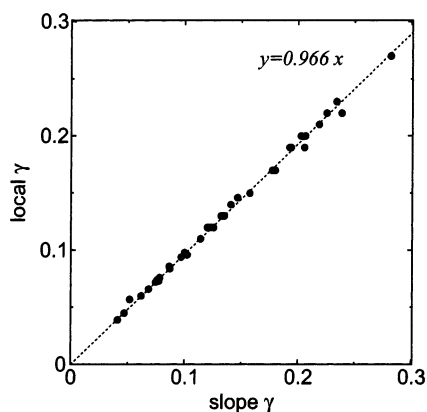


Figure 8. Correlation of the uptake coefficients defined by eq 6 (“slope γ ”) and by the uptake amount into droplets (“local γ ”). The dotted line denotes the least-squares fitting.

Figure 8 displays all the calculated data of the slope γ and local γ , indicating a very good correlation, while the slope γ generally exceeds the local γ . In this figure, the deviation is 3–4% on average and $\sim 10\%$ at maximum. Because the average deviation is small, the use of eq 6 based on the plug flow treatment can be considered adequate in this case.

The difference between the slope γ and the local γ can be attributed to the fact that the average gas velocity v_g is not identical to the average velocity of gas-phase solute species v_{solute} .⁴⁵ These velocities can be readily evaluated by the fluid dynamics simulation as

$$v_g = \frac{\int_0^{R_{\text{tube}}} v(r, Z) 2\pi r \, dr}{\int_0^{R_{\text{tube}}} 2\pi r \, dr} \quad (9)$$

$$v_{\text{solute}} = \frac{\int_0^{R_{\text{tube}}} v(r, Z) C(r, Z) 2\pi r \, dr}{\int_0^{R_{\text{tube}}} C(r, Z) 2\pi r \, dr} \quad (10)$$

where $v(r, Z)$ and $C(r, Z)$ are the axial gas velocity and the trace gas concentration at the radial and axial point (r, Z) . Using the radial concentration and velocity profiles in Figure 5, v_g and v_{solute} are calculated to be 3.80 and 3.73 m/s, respectively, showing only a 2% deviation.

The relation $v_g > v_{\text{solute}}$ elucidates the tendency for the slope γ to exceed the local γ , and it is attributed to the fact that the strongly perturbed region near the droplets has a larger gas velocity and a smaller concentration than the radially averaged values. In an overall sense, the deviation being small indicates that the strongly perturbed region in the vicinity of the axis occupies a relatively small fraction of the radial cross section of the flow tube.

However, there are some ramifications of this small breakdown in the plug-flow approximation. There is a trend in the comparison between slope γ and local γ : the deviation increases the higher the uptake on the droplets. For example, the experiments with unity α for droplet configuration A show an average deviation of $\sim 7\%$, whereas the low α (0.23) with droplet configuration C show on average no deviation between slope γ and local γ . This close investigation of the flow reactor indicates that the data analysis can have a dependence on experimental conditions. The deviation from the plug-flow approximation depends on the uptake rate on the droplets in a manner that is consistent with the radial gradients in this region.

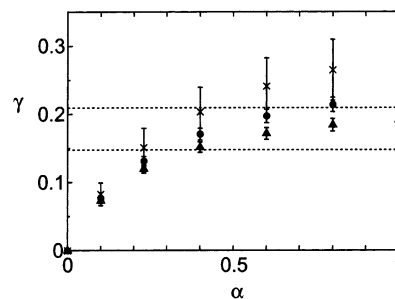


Figure 9. Calculated uptake coefficient γ as a function of the input mass accommodation coefficient α at $\text{Kn}^{\text{eff}} = 0.35$. The circles and triangles correspond to the configurations A and B, respectively, as shown in Table 1. The crosses to the difference between A and B, as discussed in the text. Two dotted lines define the range of experimentally measured γ by Li et al.⁸ at $\text{Kn}^{\text{eff}} = 0.37$ (see Figure 7).

3.2.7. Possible Range of Water α . In the above discussion, we have suggested that the experimentally measured γ is consistent with a water α that is close to 1. Here we quantify this argument and determine a possible range for the water α using the gas-phase diffusion resistance from the simulation. We calculated γ with a variable input α at $\text{Kn}^{\text{eff}} = 0.35$, which is comparable to the experimental (Kn^{eff} of 0.37, as shown in Figure 7). The experimental upper and lower limits⁸ are shown as the dashed lines. A value for Kn^{eff} of 0.35 corresponds to total pressure of 13 Torr and a He buffer gas.

The droplet train experiments are usually performed by varying the orifice frequency, and thereby surface area, while the change in the gas-phase concentration of the trace gas is monitored. Accordingly, eq 6 is modified to a differential formula,

$$\Delta k_{\text{ov}} = \frac{1}{F_g} \Delta \left(\frac{\pi d^2}{d_c} \right) \frac{\bar{c}}{4} \gamma_{\text{diff}} \quad (11)$$

When we take the difference between the results for configuration A and B in eq 11, the uncertainty in γ_{diff} , shown in the crosses in Figure 9, is enhanced over that for γ_{calc} .

Figure 9 shows the relation between the input value for α and the calculated γ 's for configurations A and B (they have the same orifice diameter and thus can be properly treated using eq 11.) Each data point from eq 6 has a numerical error of 5%, as estimated in section 3.2.5, but the frequency switching value from eq 11 has larger uncertainty ($\sim 15\%$) than this. It should be clear from Figure 9 that the differential technique is at least partly responsible for the experimental γ exceeding the simulation values, given by eq 6, for $\alpha = 1$ and droplet configuration C.

For the quantitative comparison between experiment and simulation, the experimental orifice diameter may provide another uncertainty, as the experimental orifice diameter is not known to better than 6-to-13 for the 30 μm orifice.³²

Another uncertainty that should be addressed is in the solubility resistance, $1/\Gamma_{\text{sol}}$ in eq 1, which is usually given as^{8,28}

$$\frac{1}{\Gamma_{\text{sol}}} = \frac{\bar{c}}{8RTH} \sqrt{\frac{\pi t}{D_1}} \quad (12)$$

where H is the Henry's law constant and D_1 is the diffusion coefficient of the solute in the liquid phase. Note that the solubility resistance depends on the interaction time t . The term $1/\Gamma_{\text{sol}}$ was neglected in the experimental analysis, because no saturation behavior in the uptake rate was observed.⁸ However, eq 12 provides a considerable amount of resistance for these

experimental conditions. The Henry's law constant H for water is estimated to be $H = 9.1 \times 10^3 \text{ M/atm}$ at $T = 273 \text{ K}$, using the vapor pressure of 611.3 Pa, i.e., neglecting the isotope effect on the vapor pressure. The diffusion coefficient D_1 is estimated to be $D_1 = 1.10 \times 10^{-9} \text{ m}^2/\text{s}$ at $T = 273 \text{ K}$ for H_2^{18}O , using eq 1 of ref 46. Then eq 12 gives $1/\Gamma_{\text{sol}} = 0.83$ at $t = 2 \text{ ms}$ and 1.66 at 8 ms. Adding in these corrections will lower the predicted γ in Figure 9. A precise estimate of the solubility resistance for these experimental conditions should be a remaining issue.

Comparing the calculated γ values with the experimental ones, a range in α of 0.2–1 is reasonable. This is a significant increase in the uncertainty of the extracted α and it is primarily due to the consideration of the many uncertainties in both the experiment and the calculations.

4. Concluding Remarks

The mass accommodation (condensation) coefficient α of water vapor into liquid water has been an important subject for some time, but controversy over the value of α still abounds. The mass accommodation dynamics/kinetics at the water surface can be straightforwardly explored with molecular dynamics (MD) scattering simulations. MD simulation involves little ambiguity in the microscopic interpretation, unlike experimental methods, provided that (i) the mass accommodation dynamics occur within a time scale that is tractable by MD (typically 10–100 ps), and (ii) the force field is sufficient and reliable. In the case of uptake onto water, both conditions are satisfied as argued in a number of previous studies. We performed the MD scattering simulation of the accommodation of water onto a liquid water surface, and obtained a value for the water α that is very close to 1. However, this result appears to be incompatible with the results of many other experiments, including those from the droplet train/flow reactor technique.

The droplet train/flow reactor technique has several unique advantages in measuring α , especially in effectively avoiding the problems of surface impurities and latent heat production. Recently this technique was applied to the water α using isotopically labeled water and yielded $\alpha = 0.23$ for H_2^{17}O uptake into liquid water at $T = 0^\circ\text{C}$, which is considerably smaller than unity. However, the current experimental analysis of the gas-phase resistance does not treat in detail some of the kinetic aspects of the experiment. This neglect introduces a considerable uncertainty in the reported results, as a basic understanding of the gas-phase flow and diffusion is scarce. The accurate estimate of gaseous resistance is particularly crucial for deriving the mass accommodation coefficient of water, where α is relatively large and the gaseous resistance in the flow tube is necessarily substantial due to the unavoidably abundant water vapor. Therefore, we performed numerical fluid dynamics simulation of the gas flow in the droplet train flow tube to quantitatively evaluate the gaseous resistance and thereby the water α . The fluid dynamics simulation reveals that the experimental results are consistent with a mass accommodation coefficient of H_2^{17}O that falls in the range between 0.2 and 1 at $T = 0^\circ\text{C}$.

The MD simulation and the analysis of the droplet train/flow tube experiment presented here provide a consistent picture for the water accommodation process, $\alpha \sim 1$, for liquid surfaces free of impurities and of nonequilibrium latent heat effects. Also, we conclude that the droplet train/flow reactor technique, in combination with the accurate evaluation of the gaseous resistance, is the experiment best able to probe the mass accommodation dynamics that are directly amenable to a microscopic interpretation.

A remaining problem between experiment and the present calculations for the water accommodation process is the uptake of D_2O . The droplet train/flow reactor experimental result for the uptake coefficient of D_2O is significantly larger than that of H_2^{17}O ,⁸ and the deuterated experiment is well described by the empirical Fuchs–Sutugin formula assuming $\alpha = 1$. An alternative explanation has been recently provided by Hanson et al.,⁴⁷ who argued that the interpretation of an enhanced uptake that is thought to be due to isotope exchange on the droplet surface, can be complicated by facile H–D exchange on the reactor wall. Further work from both experimental and theoretical sides is needed to fully elucidate the uptake kinetics due to isotope exchange on surfaces.

Acknowledgment. The authors thank Drs. Mitsuhiro Matsumoto, Doug Worsnop, Paul Davidovits, Chuck Kolb and Jun Hirokawa for stimulating discussion and useful comments. This work was supported by Grants-in-Aid (Grant Nos. 13127104, 13740329, 14048216) from the Ministry of Education and Science, Japan, and from AGS (Alliance for Global Sustainability) Project “Regional Climate and Air Quality”.

References and Notes

- (1) Pruppacher, H. R.; Klett, J. D. *Microphysics of Clouds and Precipitation*; Reidel: Dordrecht, 1978.
- (2) Wagner, P. E. Aerosol Growth by Condensation. In *Aerosol Microphysics II, Chemical Physics of Microparticles*; Marlow, W. H., Ed.; Springer-Verlag: Berlin, 1982.
- (3) Mozurkewich, M. *Aerosol Sci. Technol.* **1986**, *5*, 223–236.
- (4) Hagen, D. E.; Schmitt, J.; Trublood, M.; Carstens, J.; White, D. R.; Alofs, D. J. *J. Atmos. Sci.* **1989**, *46*, 803–816.
- (5) Marek, R.; Straub, J. *Int. J. Heat Mass Transfer* **2001**, *44*, 39–53.
- (6) Bigg, E. K. *Atmos. Res.* **1986**, *20*, 81–86.
- (7) Seinfeld, J. H.; Pandis, S. N. *Atmospheric Chemistry and Physics*; Wiley: New York, 1998.
- (8) Li, Y. Q.; Davidovits, P.; Shi, Q.; Jayne, J. T.; Kolb, C. E.; Worsnop, D. R. *J. Phys. Chem. A* **2001**, *105*, 10627–10634.
- (9) Townsend, R. M.; Gryko, J.; Rice, S. A. *J. Chem. Phys.* **1985**, *82*, 4391–4392.
- (10) Matsumoto, M.; Kataoka, Y. *J. Chem. Phys.* **1988**, *88*, 3233–3245.
- (11) Wilson, M. A.; Pohorille, A.; Pratt, L. R. *J. Phys. Chem.* **1987**, *91*, 4873–4878.
- (12) Wilson, M. A.; Pohorille, A.; Pratt, L. R. *J. Chem. Phys.* **1988**, *88*, 3281–3285.
- (13) Alejandre, J.; Tildesley, D. J.; Chapela, G. A. *J. Chem. Phys.* **1995**, *102*, 4574–4583.
- (14) Taylor, R. S.; Dang, L. X.; Garrett, B. C. *J. Phys. Chem.* **1996**, *100*, 11720–11725.
- (15) Benjamin, I.; Wilson, M. A.; Pohorille, A. *J. Chem. Phys.* **1994**, *100*, 6500–6507.
- (16) Benjamin, I.; Wilson, M. A.; Pohorille, A.; Nathanson, G. M. *Chem. Phys. Lett.* **1995**, *243*, 222–228.
- (17) Wilson, M. A.; Pohorille, A. *J. Phys. Chem. B* **1997**, *101*, 3130–3135.
- (18) Taylor, R. S.; Ray, D.; Garrett, B. C. *J. Phys. Chem. B* **1997**, *101*, 5473–5476.
- (19) Taylor, R. S.; Garrett, B. C. *J. Phys. Chem. B* **1999**, *103*, 844–851.
- (20) Somasundaram, T.; in het Panhuis, M.; Lyndel-Bell, R. M.; Patterson, C. H. *J. Chem. Phys.* **1999**, *111*, 2190–2199.
- (21) Matsumoto, M. *Fluid Phase Equil.* **1998**, *144*, 307–314.
- (22) Nagayama, G.; Tsuruta, T. *J. Chem. Phys.* **2003**, *118*, 1392–1399.
- (23) Morita, A. *Chem. Phys. Lett.* **2003**, *375*, 1–8.
- (24) Saecker, M. E.; Nathanson, G. M. *J. Chem. Phys.* **1993**, *99*, 7056–7089.
- (25) Jayne, J. T.; Duan, S. X.; Davidovits, P.; Worsnop, D. R.; Zahniser, M. S.; Kolb, C. E. *J. Phys. Chem.* **1991**, *95*, 6329–6336.
- (26) Shi, Q.; Li, Y. Q.; Davidovits, P.; Jayne, J. T.; Worsnop, D. R.; Mozurkewich, M.; Kolb, C. E. *J. Phys. Chem. B* **1999**, *103*, 2417–2430.
- (27) Katrib, Y.; Mirabel, P.; Calvé, S. L.; Weck, G.; Kochanski, E. *J. Phys. Chem. B* **2002**, *106*, 7237–7245.
- (28) Kolb, C. E.; Worsnop, D. R.; Zahniser, M. S.; Davidovits, P.; Keyser, L. F.; Leu, M. T.; Molina, M. J.; Hanson, D. R.; Ravishankara, A. R. Laboratory Studies of Atmospheric Heterogeneous Chemistry. In *Progress and Problems in Atmospheric Chemistry*; Baker, J. R., Ed.; World Scientific: Singapore, 1995.

- (29) Fuchs, N. A.; Sutugin, A. G. *Highly Dispersed Aerosols*; Ann Arbor Science Publishers: Ann Arbor, 1970.
- (30) Worsnop, D. R.; Zahniser, M. S.; Kolb, C. E.; Gardner, J. A.; Watson, L. R.; Van Doren, J. M.; Jayne, J. T.; Davidovits, P. *J. Phys. Chem.* **1989**, *93*, 1159–1172.
- (31) Swartz, E.; Shi, Q.; Davidovits, P.; Jayne, J. T.; Worsnop, D. R.; Kolb, C. E. *J. Phys. Chem. A* **1999**, *103*, 8824–8833.
- (32) Worsnop, D. R.; Shi, Q.; Jayne, J. T.; Kolb, C. E.; Swartz, E.; Davidovits, P. *J. Aerosol Sci.* **2001**, *32*, 877–891.
- (33) Sugiyama, M.; Koda, S.; Morita, A. *Chem. Phys. Lett.* **2002**, *362*, 56–62.
- (34) Morita, A.; Sugiyama, M.; Koda, S. *J. Phys. Chem. A* **2003**, *107*, 1749–1759.
- (35) Frenkel, D.; Smit, B. *Understanding Molecular Simulation*; Academic Press: San Diego, 1996.
- (36) Berendsen, H. J. C.; Grigera, J. R.; Straatsma, T. P. *J. Phys. Chem.* **1987**, *91*, 6269–6271.
- (37) Allen, M. P.; Tildesley, D. J. *Computer Simulation of Liquids*; Oxford University Press: New York, 1987.
- (38) More exactly, the initial Z coordinate of a generated molecule is set to $Z = \pm (L/2 + 15 \text{ \AA})$, where the origin $Z = 0$ corresponds to the center of mass of the film.
- (39) Lide, D. R., Ed.; *Handbook of Chemistry and Physics*; CRC Press: Boca Raton, 81st ed.; 2000.
- (40) Kee, R. J. et al. *Chemkin Collection, Release 3.6*; Reaction Design, Inc.: San Diego, CA, 2001.
- (41) Morita, A.; Sugiyama, M.; Koda, S. *J. Phys. Chem. A* **2004**, in press.
- (42) Worsnop, D. R.; Williams, L. R.; Kolb, C. E.; Mozurkewich, M.; Gershenzon, M.; Davidovits, P. *J. Phys. Chem. A* **2004**, in press.
- (43) Ibuki, K.; Ueno, M. *Bull. Chem. Soc. Jpn.* **1997**, *70*, 543–553.
- (44) *FLUENT ver 6*; Fluent, Inc.: Lebanon, NH, 2002 <http://www.fluent.com/>.
- (45) Howard, C. J. *J. Phys. Chem.* **1979**, *83*, 3–9.
- (46) Eastal, A. J.; Vernon, A.; Edge, J.; Woolf, L. A. *J. Phys. Chem.* **1984**, *88*, 6060–6063.
- (47) Hanson, D. R.; Sugiyama, M.; Morita, A. *J. Phys. Chem. A* **2004**, *108*, 3739–3744.